nanomaterials

MDPI

Article

Synchronous Defect and Interface Engineering of $NiMoO_4$ Nanowire Arrays for High-Performance Supercapacitors

Pengcheng Wang [1], Xinying Ding [1], Rongjie Zhe [1], Ting Zhu [1,2], Chen Qing [1,2,*], Yingkai Liu [1] and Hong-En Wang [1,2,*]

[1] Yunnan Key Laboratory of Optoelectronic Information Technology, College of Physics and Electronics Information, Yunnan Normal University, Kunming 650500, China; pcwang0312@163.com (P.W.); xinyingding1998@163.com (X.D.); rongjiezhe@163.com (R.Z.); zhut0002@ynnu.edu.cn (T.Z.); ykliu@ynnu.edu.cn (Y.L.)

[2] Key Laboratory of Advanced Technique & Preparation for Renewable Energy Materials, Ministry of Education, Yunnan Normal University, Kunming 650500, China

* Correspondence: qingchen1@126.com (C.Q.); hongenwang@whut.edu.cn (H.-E.W.)

Abstract: Developing high-performance electrode materials is in high demand for the development of supercapacitors. Herein, defect and interface engineering has been simultaneously realized in $NiMoO_4$ nanowire arrays (NWAs) using a simple sucrose coating followed by an annealing process. The resultant hierarchical oxygen-deficient $NiMoO_4$@C NWAs (denoted as "$NiMoO_{4-x}$@C") are grown directly on conductive ferronickel foam substrates. This composite affords direct electrical contact with the substrates and directional electron transport, as well as short ionic diffusion pathways. Furthermore, the coating of the amorphous carbon shell and the introduction of oxygen vacancies effectively enhance the electrical conductivity of $NiMoO_4$. In addition, the coated carbon layer improves the structural stability of the $NiMoO_4$ in the whole charging and discharging process, significantly enhancing the cycling stability of the electrode. Consequently, the $NiMoO_{4-x}$@C electrode delivers a high areal capacitance of 2.24 F cm^{-2} (1720 F g^{-1}) at a current density of 1 mA cm^{-2} and superior cycling stability of 84.5% retention after 6000 cycles at 20 mA cm^{-2}. Furthermore, an asymmetric super-capacitor device (ASC) has been constructed with $NiMoO_{4-x}$@C as the positive electrode and activated carbon (AC) as the negative electrode. The as-assembled ASC device shows excellent electrochemical performance with a high energy density of 51.6 W h kg^{-1} at a power density of 203.95 W kg^{-1}. Moreover, the $NiMoO_4$//AC ASC device manifests remarkable cyclability with 84.5% of capacitance retention over 6000 cycles. The results demonstrate that the $NiMoO_{4-x}$@C composite is a promising material for electrochemical energy storage. This work can give new insights on the design and development of novel functional electrode materials via defect and interface engineering through simple yet effective chemical routes.

Keywords: $NiMoO_4$ nanowire arrays; oxygen vacancies; core-shell electrode structure; asymmetric supercapacitors

Citation: Wang, P.; Ding, X.; Zhe, R.; Zhu, T.; Qing, C.; Liu, Y.; Wang, H.-E. Synchronous Defect and Interface Engineering of $NiMoO_4$ Nanowire Arrays for High-Performance Supercapacitors. *Nanomaterials* **2022**, *12*, 1094. https://doi.org/10.3390/nano12071094

Academic Editors: Jihoon Lee and Ming-Yu Li

Received: 1 March 2022
Accepted: 24 March 2022
Published: 26 March 2022

1. Introduction

Several alternative energy technologies have been under development globally in a great effort to mitigate the energy and environmental challenges faced and in accordance with the current "carbon neutral" policies. Supercapacitors (SCs), also known as electrochemical capacitors (ECs), have been considered as one of the most promising energy storage devices due to their unique characteristics of high power density (>10 kW/kg), fast charging and discharging capability (within a few seconds), long lifespan (over 100,000 cycles), and good operational safety. SCs have been widely applied in some important fields, including smart electric grids, memory back-ups, (hybrid) electric vehicles, and aerospace crafts. Although SCs have the advantages of high power density and very long calendar lives, their further application is still hindered by their limited energy density.

Therefore, it is crucial to develop advanced high-performance SCs with higher energy densities without severely compromising the power density and cyclability.

Recently, asymmetric supercapacitors (ASCs) have been regarded as promising due to their enhanced energy density. ASCs commonly combine pseudocapacitive materials (as positive electrode) and electric double-layer capacitive materials (as negative electrode), making use of the much higher specific capacitance derived from the pseudocapacitive electrode materials and a wider potential window during operation. In this sense, the electrochemical performances of ASCs are largely influenced by the structures and properties of the pseudocapacitive electrode materials. Thus, the development of high energy density ASCs heavily relies on the rational selection and design, as well as delicate fabrication of advanced electrode materials.

The use of transition metal oxides (TMOs) [1], hydroxides [2], sulfides [3], selenides [4], carbides [5], and their composites with conductive carbon and polymers [6], as possible electrode materials for ASCs, has been attempted. Particularly, TMOs, such as NiO [7], MoO_3 [8], Co_3O_4 [9], and MnO_2 [10], have received considerable attention due to their low cost, convenience of synthesis, environmental friendliness, and relatively high capacitance. Compared to binary TMOs, ternary TMOs materials containing two different metal cations, such as $NiCo_2O_4$ [11], $ZnCo_2O_4$ [12,13], $CoMoO_4$ [14], $MnMoO_4$ [15], and $NiMoO_4$ [16], as well as some solid solutions [17], exhibit higher electrochemical activity due to the rich redox reactions stemming from the multiple oxidation states of the transition-metal components. It has been proposed that $NiMoO_4$ has a good reversible capacitance and electrochemical characteristics for SCs/ASCs applications because of the electrochemical active Ni cation and improved electronic conductivity from Mo cation [16,18].

However, the practical application of $NiMoO_4$ electrodes in SCs and ASCs is still hampered by their poor electronic conductivity, insufficient ionic transport and diffusion, and structural instability during long-term cycling [19]. Therefore, the controllable fabrication of $NiMoO_4$ with desired nano- and microstructures and rational structural engineering is highly desired but remains challenging.

Various nanostructured $NiMoO_4$ materials, such as nanosheets and nanorods arrays [20], nanotubes [21], hollow nanorods [22], mesoporous nanospheres [23], nanoparticles, and quantum dots [24], have been designed to boost the electrochemical performances of the $NiMoO_4$ electrodes via increased exposed surface for ion adsorption and insertion, shortened path distances for ion transport and diffusion, and improved electrolyte impregnation and permeation. Specifically, various low-dimensional $NiMoO_4$ nanostructures directly grown on conductive substrates (e.g., Ni/Cu foams [25,26], graphene [27], and carbon substrates [28,29]) are particularly preferred for directional electron transport with reduced charge carrier scattering at grain boundaries and easy integration into flexible devices with some specific applications.

To overcome the poor electronic conductivity of pristine $NiMoO_4$, various $NiMoO_4$/carbon composites have been synthesized by hybridizing $NiMoO_4$ nanostructures with graphene [30,31], carbon nanotubes [32], conducting polymers [33], and porous carbon architectures [34,35] Alternatively, intentional doping of $NiMoO_4$ with several kinds of heteroatoms such as Mn [36,37], P [38], Zn [39], Ce [40], or the creation of oxygen vacancies [14,41–43] in the lattice have recently been reported. In addition, $NiMoO_4$ has also been coupled with other metal oxides [44–49] or sulfides [50–52] to form heterostructure electrodes for supercapacitors with improved electrochemical performances.

However, monotonous strategy sometimes has a limited contribution for the overall electrochemical performance improvement of $NiMoO_4$ materials. In addition, some reported approaches for hybridization or doping of $NiMoO_4$ involve multiple and complex chemical and physical processes that are not economically or environmentally friendly. Thus, the rational design and the design of a $NiMoO_4$-based composite electrode for high-performance supercapacitors remains a challenge.

In this work, we report the simultaneous defect and interface engineering of $NiMoO_4$ nanowires arrays (NWAs) using a simple and effective sucrose coating followed by a

thermal treatment approach. In this process, an amorphous carbon shell was uniformly coated on the $NiMoO_4$ surface, effectively improving the electronic transport and structural integrity of the $NiMoO_4$ during electrochemical cycling. Additionally, oxygen-vacancy defects were incorporated into the $NiMoO_4$ during the carbonization process, further enhancing the electronic conductivity of $NiMoO_4$ and redox activity in the $NiMoO_4$ electrode surface. As expected, the resultant $NiMoO_{4-x}$@C composite exhibited a higher specific capacitance than that of the pristine $NiMoO_4$ NWAs. Furthermore, an asymmetric supercapacitor (ASC) was assembled with the $NiMoO_{4-x}$@C as positive electrode and activated carbon (AC) as negative electrode, delivering a remarkably high energy density of 51.6 W h kg^{-1} at a power density of 203 W kg^{-1} and an excellent cycling stability with a retention of 84.5% after 6000 cycles under a high current density of 10 A g^{-1}.

2. Results and Discussion

The synthesis route of oxygen-deficient $NiMoO_4$@carbon nanowire arrays ($NiMoO_{4-x}$@C) is schematically shown in Figure 1. The preparation process mainly involved three critical steps. Firstly, a $NiMoO_4$ nanowire arrays (NWAs) precursor ($NiMoO_4 \cdot xH_2O$ NWAs, light green) was directly deposited on a ferronickel foam by a hydrothermal reaction process (Step 1, Figure 1). Secondly, the $NiMoO_4$ NWAs precursor was transferred into $NiMoO_4$ NWAs by annealing in Ar to remove crystal H_2O and improve crystallinity (Step 2, Figure 1). Finally, the as-obtained $NiMoO_4$ NWAs were immersed in a sucrose solution, followed by drying and annealing in an Ar atmosphere to fabricate oxygen-deficient $NiMoO_4$@carbon NWAs ($NiMoO_{4-x}$@C) (Step 3, Figure 1).

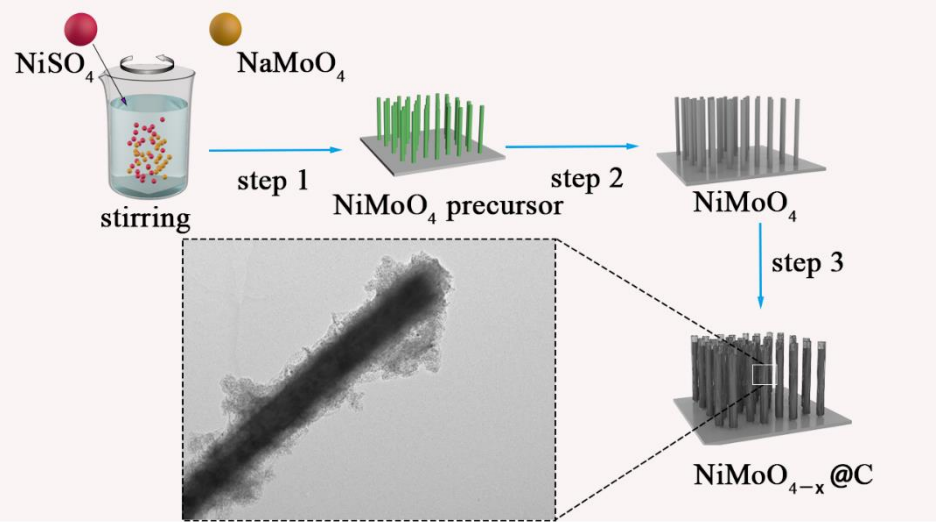

Figure 1. Schematic illustration of the synthesis process of oxygen-deficient $NiMoO_4$@carbon nanowire arrays (NWAs) (denoted as "$NiMoO_{4-x}$@C"). Step 1, growth of the $NiMoO_4$ NWAs precursor directly on a ferronickel foam substrate using a hydrothermal process; Step 2, conversion of the $NiMoO_4$ NWAs precursor into the $NiMoO_4$ NWAs via annealing in Ar; Step 3, fabrication of $NiMoO_{4-x}$@C composite by sucrose coating followed by annealing in Ar.

The crystal structures of $NiMoO_{4-x}$@C and neat $NiMoO_4$ NWAs samples were characterized by X-ray diffraction (XRD) analysis as depicted in Figure 2. The two strongest diffraction peaks, located at ca. 45° and 52°, were from the ferronickel foam substrate. The $NiMoO_{4-x}$@C and $NiMoO_4$ NWAs samples showed similar diffraction peak shapes and locations. The diffraction peaks located at 14.3°, 24.0°, 25.4°, 28.9°, 32.6°, 37.1°, 38.7°, 41.3°, and 47.4° corresponded to the (110), (021), (−112), (220), (022), (−113), (−132), (040), and (−204) crystal planes of orthorhombic $NiMoO_4$ (JCPDS card No. 86-0361) [37]. Compared to the $NiMoO_4$ NWAs samples, the $NiMoO_{4-x}$@C sample exhibited a slightly lower diffraction peak intensity possibly due to the covering of carbon on the $NiMoO_4$ surface as well

as the reduced crystallinity of $NiMoO_4$ with increased structural defects. In addition, no characteristic peaks for carbon phases were noted, suggesting the amorphous nature of the carbon species in the $NiMoO_{4-x}$@C sample. The formation of amorphous carbon could be partially ascribed to the lower low annealing temperature (400 °C herein).

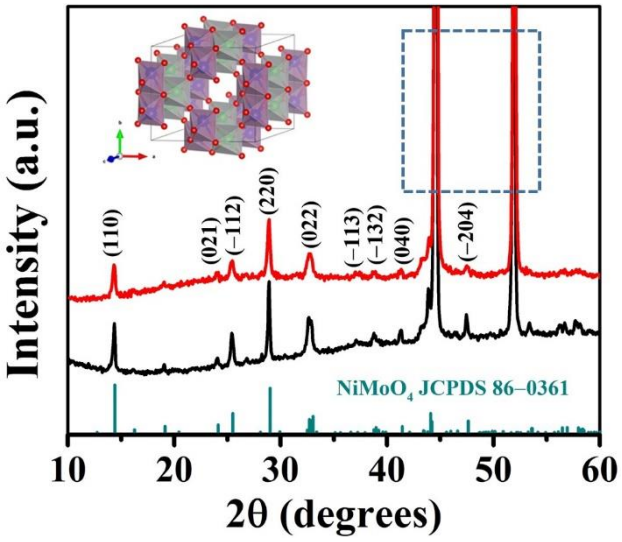

Figure 2. XRD patterns of $NiMoO_4$ NWAs (black) and $NiMoO_{4-x}$@C composite (red). The inset (top left) shows the structural model of $NiMoO_4$ crystal, whereas the green, blue, and red balls represent the Ni, Mo, and O atoms, respectively. The two strongest diffraction peaks in the square regions of dotted line are from the ferronickel foam substrate.

Raman spectra of pristine $NiMoO_4$ NWAs and $NiMoO_{4-x}$@C samples are illustrated in Figure 3. The bands at 961 cm^{-1} and 913 cm^{-1} corresponded to the symmetric and asymmetric stretching modes of Mo=O bonds, while the band at 706 cm^{-1} could be ascribed to the stretching mode of Ni/Mo-O bonds of the orthorhombic α-$NiMoO_4$ phase [53]. In addition, two bands ascribed to the presence of carbon species were identified. The band at around 1360 cm^{-1} could be attributed to the D band from defects and disorders in the amorphous carbon layers, while the other band at around 1590 cm^{-1} was related to the G band related to the vibration of sp^2-bonded carbon atoms [54]. This result implied the successful deposition of amorphous carbon layer on the surface of the $NiMoO_4$ NWAs.

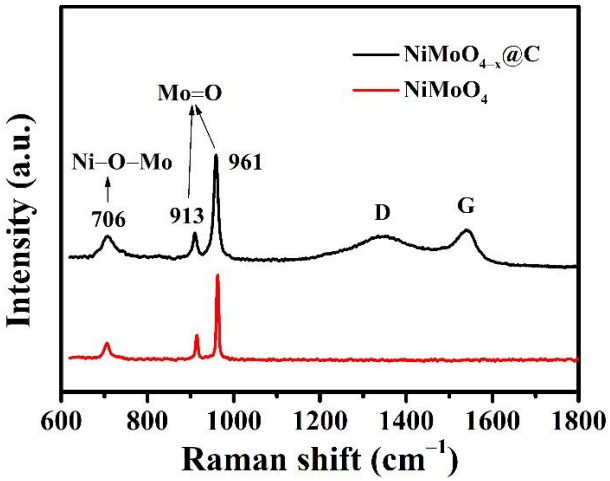

Figure 3. Raman spectra of $NiMoO_{4-x}$@C (black) and pristine $NiMoO_4$ NWAs (red) samples.

The morphologies of the $NiMoO_4$ samples were firstly observed using scanning electron microscopy (SEM). From Figure 4a, the pristine $NiMoO_4$ NWAs sample was

composed of oriented nanowires (NWs) with a smooth surface. In addition, the $NiMoO_4$ NWAs have relatively uniform diameters of ~300 nm, on average, and lengths of several micrometers. After the coating of the carbon, the surface of the $NiMoO_{4-x}$@C sample became obviously coarse as shown in Figure 4b. The element composition analyses using energy-dispersive X-ray spectra (EDS) analysis indicated the existence of Ni, Mo, O, C, Fe, and Al elements in the $NiMoO_{4-x}$@C sample (Figure S1, Supporting Information). Note that the Fe and Al signals mainly stemmed from the ferronickel foam substrate and the sample holder, respectively.

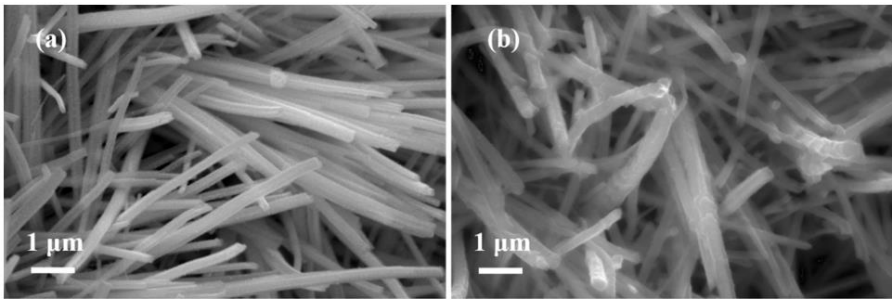

Figure 4. SEM images of (**a**) neat $NiMoO_4$ NWAs and (**b**) $NiMoO_{4-x}$@C samples.

The microstructures of the pure $NiMoO_4$ NWAs and $NiMoO_{4-x}$@C samples were further investigated by transmission electron microscope (TEM) and high-resolution TEM (HRTEM) as shown in Figure 5. The TEM image (Figure 5a) revealed that the pure $NiMoO_4$ nanowire had a smooth surface with a diameter of about 200 nm. A selected-area electron diffraction (SAED) pattern (inset of Figure 5a) taken from this nanowire depicted a clear two-dimensional dot pattern, suggesting its single-crystalline structure in nature. Two diffraction spots, as marked by white circles, could be indexed to the (220) and (−222) crystal facets of orthorhombic $NiMoO_4$. From Figure 5b, the crystal plane with a lattice spacing of 2.73 Å in the HRTEM micrograph corresponded to the (−222) planes of $NiMoO_4$ [49,52]. In contrast, the TEM image in Figure 5c indicated that a layer of amorphous carbon film with a thickness of ca. 20~50 nm had been coated on the $NiMoO_4$ nanowire's surface, confirming the core-shell structure of the $NiMoO_{4-x}$@C composite sample with different brightness contrasts of $NiMoO_4$ and carbon. The deposition of amorphous carbon on the surface of $NiMoO_4$ can be further confirmed by HRTEM micrograph as shown in Figure 5d.

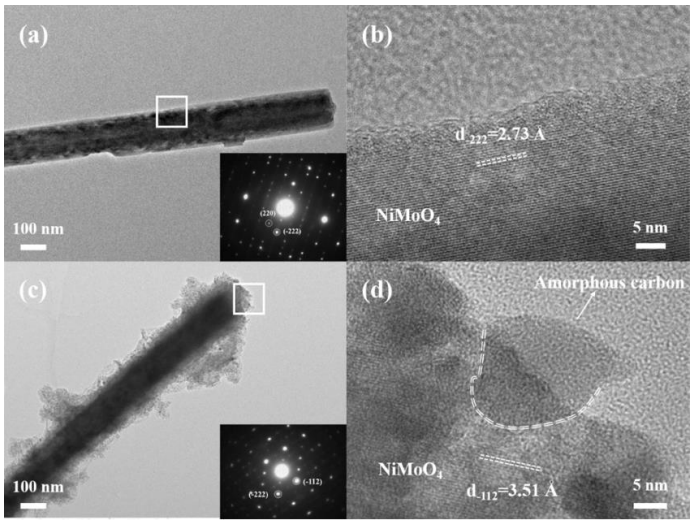

Figure 5. TEM images (**a**,**c**) and HRTEM micrographs (**b**,**d**) of pure $NiMoO_4$ NWAs (**a**,**b**) and $NiMoO_{4-x}$@C (**c**,**d**) samples. The insets in (**a**,**c**) are corresponding SAED patterns taken from a single nanowire.

Next, the chemical composition and valence states of element on the surface of $NiMoO_4$ NWAs and $NiMoO_{4-x}$@C samples were identified by X-ray photoelectron spectroscopy (XPS, Figure 6). In the high-resolution Ni 2p spectrum of the pristine $NiMoO_4$ NWAs sample (Figure 6a), two main peaks were observed at binding energies (BEs) of 873.4 eV and 856.3 eV with a spin-orbital splitting energy of 17.1 eV, corresponding to the Ni $2p_{1/2}$ and Ni $2p_{3/2}$ of Ni^{2+} in $NiMoO_4$ lattice [55]. In addition, two satellite peaks with BEs of 877.3 eV and 860.6 eV were noted for Ni^{2+}. In Figure 6b, similar peak locations and separations can also be observed in the Ni 2p spectra of $NiMoO_{4-x}$@C sample, indicating the coating of carbon had little effect on the chemical valence states of the Ni component in $NiMoO_4$. The Mo 6d spectrum of pure $NiMoO_4$ and $NiMoO_{4-x}$@C samples are shown in Figure 6c,d. Evidently both samples had two strong bands with BEs located at 236.0 eV and 232.9 eV, which could be assigned to Mo $3d_{3/2}$ and Mo $3d_{5/2}$ of Mo^{6+} cations in the $NiMoO_4$ lattice [56]. In addition, another pair of doublets was noted for the $NiMoO_{4-x}$@C sample, verifying the existence of Mo^{4+} in the $NiMoO_{4-x}$@C composite [41,42,57] possibly produced during the amorphous carbon coating process. From Figure 6e, the O 1s spectrum of the $NiMoO_4$ NWs sample was deconvoluted into three bands. The band centered at 530.1 eV was assigned to the lattice oxygen with O-Ni/O-Mo bonds, while the bands located at 531.3 eV and 532.9 eV correspond to the O-C and O=C bonds from moisture adsorbed on surface [58]. For the $NiMoO_{4-x}$@C sample, another band could be noted at 532 eV, suggesting the presence of oxygen vacancies (V_o) [59] at the $NiMoO_4$ surface (Figure 6f). The formation of and Mo^{4+} and V_o can tune the electronic structures and electrochemical properties of the $NiMoO_{4-x}$@C composite sample.

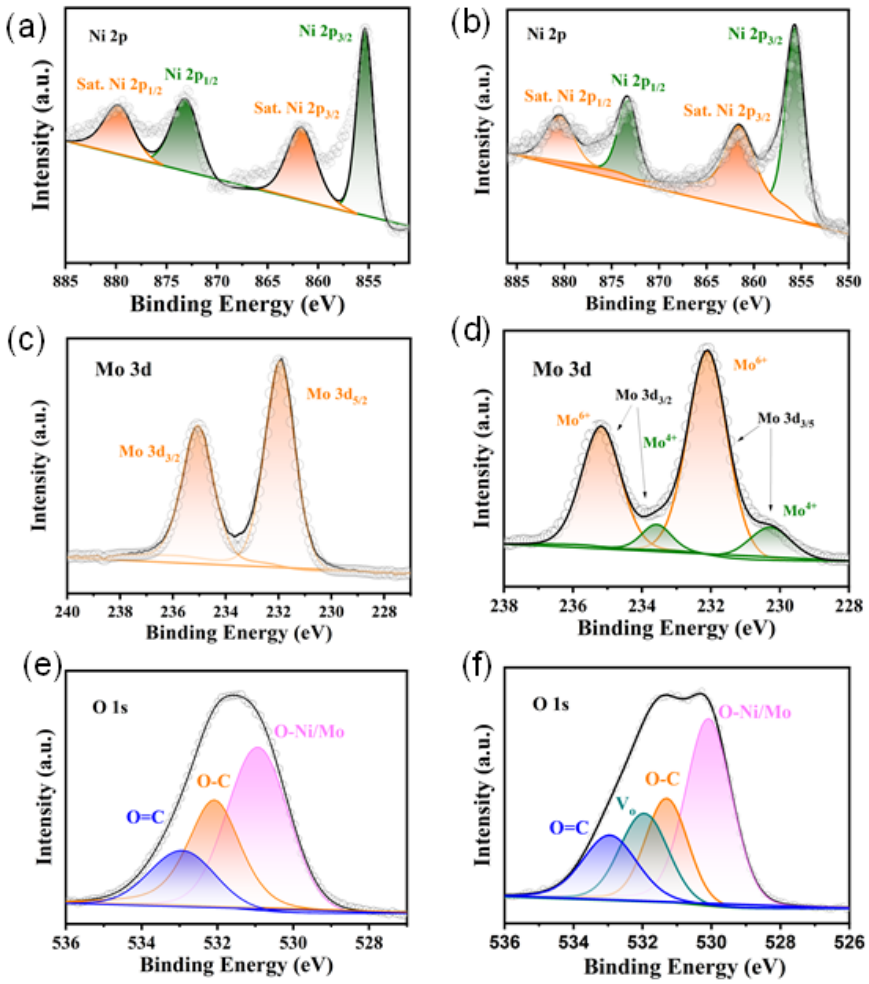

Figure 6. High-resolution XPS spectra of (**a**,**c**,**e**) pristine $NiMoO_4$ and (**b**,**d**,**f**) $NiMoO_{4-x}$@C samples; (**a**,**b**) Ni 2p, (**c**,**d**) Mo 3d, (**e**,**f**) O 1s.

Then, the effects of pyrolysis temperatures (from 200~800 °C) during the carbon coating of the morphologies and microstructures of the $NiMoO_4$/carbon composites were investigated. It is noted that some aggregates of residual sucrose were observed after annealing at 200 °C (Figure S2a), suggesting the carbonization of sucrose was incomplete under a lower temperature. This SEM result also coincides well with the thermogravimetric (TGA) and the differential scanning calorimetry (DSC) analyses (Figure S3), where the thermal decomposition process of sucrose mainly occurs between 223 and 389 °C. With the increase of annealing temperature, sucrose was decomposed, and the carbonization process occurred accompanied by the release of some gases (e.g., CO, CO_2). At a higher temperature, the generated reductive gases (e.g., CO) reacted with $NiMoO_4$ and generated some oxygen vacancies on the $NiMoO_4$ surface via abstracting some surface oxygen atoms. In contrast, well-defined nanowires were obtained for the samples prepared after annealing at 400 and 600 °C, respectively (Figure S2b,c). However, the nanowire structure was destroyed when the pyrolysis temperature was increased to 800 °C (Figure S2d), which might have been caused by the large inner stain in the $NiMoO_4$ NWAs or at the $NiMoO_{4-x}$@C interface. Thus, the standard annealing temperature was chosen as 400 °C.

To evaluate the electrochemical performance of $NiMoO_4$ NWAs and $NiMoO_{4-x}$@C samples, electrochemical measurements were tested by a three-electrode system with 2 M KOH electrolyte (Figure 7). Figure 7a shows the CV curves of $NiMoO_4$ NWAs and $NiMoO_{4-x}$@C samples at a scan rate of 20 mV s^{-1} with a potential window of 0 to 0.7 V. Overall, the $NiMoO_{4-x}$@C sample had a larger integral area than that of the $NiMoO_4$ NWAs sample, indicating a significant increase of capacitance after carbon deposition and introduction of oxygen vacancies. Meanwhile, the CV curves of the two samples exhibited typical oxidation peaks, demonstrating typical pseudocapacitive charge storage characteristics. In addition, the CV curves of four different pyrolysis temperatures of $NiMoO_{4-x}$@C samples are revealed in Figure S4. The sample collected at 400 °C shows the highest capacitance which is consistent with the result of SEM in Figure S2. The sample collected at 800 °C exhibited an unsatisfactory performance due to its collapsed morphology. Figure 7b shows the GCD curves of the two samples. It revealed that the discharge time of the $NiMoO_{4-x}$@C sample was almost twice as much as that of the $NiMoO_4$ NWAs sample at a current density of 1 A cm^{-2}. Figure 7c shows the electrochemical impedance spectroscopy (EIS) of $NiMoO_4$ NWAs and $NiMoO_{4-x}$@C. The direct impedance and charge transfer resistance of the $NiMoO_{4-x}$@C sample was significantly lower than that of the $NiMoO_4$ NWAs sample. The remarkably reduced size of the semicircle for the $NiMoO_{4-x}$@C indicated an improved charge transfer kinetics due to enhanced electrical conductivity provided by the carbon shell and oxygen vacancy defects. In addition, the $NiMoO_{4-x}$@C exhibits the steepest slope in the low-frequency region, clearly indicating the lowest Warburg impedance and, hence, the highest K-ion diffusion capability at the interface between the electrode and electrolyte. Through the AC EIS, we added the corresponding equivalent circuit diagram in Figure 7c.

The true impedance of capacitor can be estimated using the following Equation (1):

$$Z_{real} = R_\Omega + \frac{-j(wC)\left(R_{ct} + W \cdot jw^{1/2}\right)}{R_{ct} + W \cdot jw^{1/2} - j(wC)} \quad (1)$$

Figure 7d shows the capacitance of $NiMoO_4$ NWAs and $NiMoO_{4-x}$@C samples calculated from different current densities. After coating the carbon layer, the capacitance of the $NiMoO_{4-x}$@C sample was greatly increased. The areal capacitance can be calculated as high as 2.24 F cm^{-2} (1720 F g^{-1}) at a current density of 1 mA cm^{-2}. In contrast, the $NiMoO_4$ NWAs electrode only demonstrated a specific capacitance of 1.206 F cm^{-2} (927 F g^{-1}) at the same current density. The cycling performances of $NiMoO_4$ NWAs and $NiMoO_{4-x}$@C samples are presented in Figure 7e. The capacitance retention of $NiMoO_{4-x}$@C is 84.5% at 20 mA cm^{-2} after 6000 cycles, which is considerably better than that of the $NiMoO_4$ NWAs sample (63.1% after 6000 cycles). To illustrate the difference of the cycling process between $NiMoO_4$ NWAs and $NiMoO_{4-x}$@C samples, we also obtained the SEM results after cycling

as shown in Figure S5. It is evident that the $NiMoO_{4-x}$@C sample still held some nanorod structures under the protection of amorphous carbon shell. Instead, $NiMoO_4$ NWAs were aggregated after 10,000 cycles, with unsatisfactory cycle abilities. In addition, we made a comparison of the C_s and cycling stability of this work with some previously reported $NiMoO_4$-based electrodes materials as summarized in Table S1.

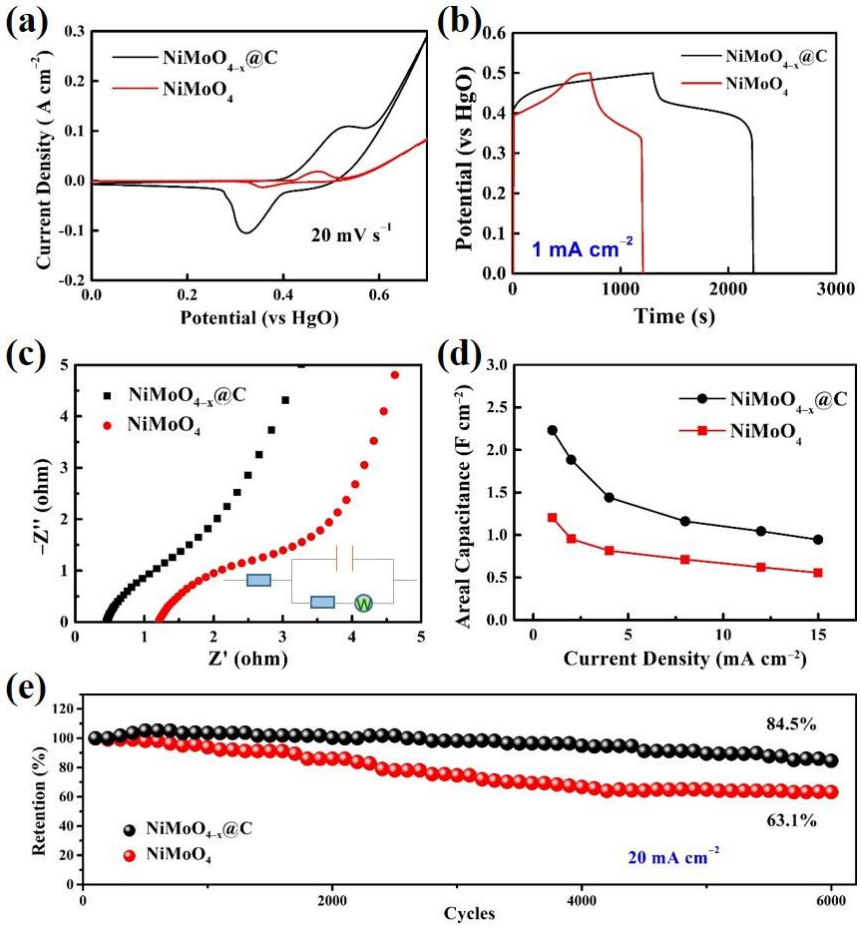

Figure 7. (**a**) CV curves of the $NiMoO_4$ NWAs and $NiMoO_{4-x}$@C at a scan rate of 20 mV s^{-1}. (**b**) GCD curves and (**c**) EIS spectra of $NiMoO_4$ NWAs and $NiMoO_{4-x}$@C and its corresponding equivalent fitting circuit. (**d**) GCD test of $NiMoO_{4-x}$@C at different current densities. (**e**) Cycle test of $NiMoO_4$ NWAs and $NiMoO_{4-x}$@C at 20 mA cm^{-2} over 6000 cycles.

First-principles density functional theory (DFT) simulations were next adopted to further probe the structure–performance relationship of the $NiMoO_{4-x}$@C composite electrode in supercapacitors. The optimized geometry configurations of pristine and oxygen-deficient $NiMoO_4$ (110) surface slabs are shown in Figure S6. The pristine $NiMoO_4$ (110) surface was flat and composed of fivefold Ni and Mo atoms and twofold O atoms (Figure S6a). The defective $NiMoO_4$ (110) surface can be produced after eliminating one surface O atom, leaving one threefold Ni and Mo atoms nearby (Figure S6b). The resultant oxygen-deficient $NiMoO_4$ (110) plane retains flat. Next, the adsorption behavior of OH group on the pristine $NiMoO_4$ (110) surface was first investigated. As shown in Figure 8, the OH can be adsorbed on the top of either the surface of the Mo atom (Figure 8a,b) or the Ni atom (Figure 8c,d), yielding an adsorption energy (E_{ads}) of −0.50 and −5.97 eV, respectively. Evidently, the adsorption of OH on the Ni site was much stronger than that on the Mo site, which is consistent with the fact that the Ni in $NiMoO_4$ is electrochemically active for pseudocapacitive charge storage process based on Faradic reactions. The chemisorption of OH on Ni and Mo sites of the $NiMoO_4$ (110) surface was further verified by the interfacial charge transfer from the charge density difference contours (Figure S7).

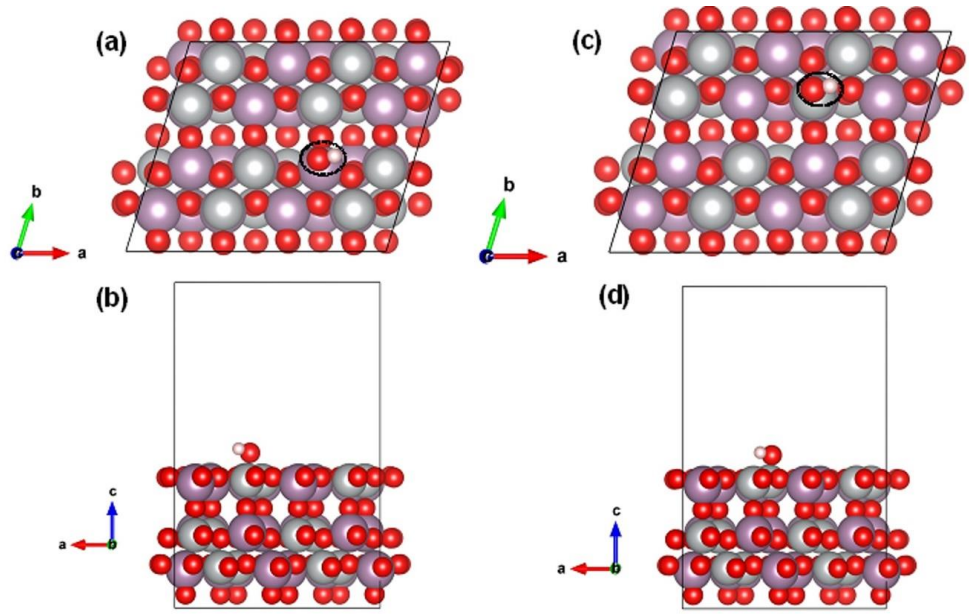

Figure 8. The optimized adsorption configurations of one HO molecule anchored on exposed (**a**,**b**) Mo- and (**c**,**d**) Ni- atoms of pristine $NiMoO_4$ (110) surfaces, leading to an E_{ads} of −0.50 and −5.97 eV, respectively. The black dotted ellipsoids in (**a**,**c**) mark the positions of the adsorbed HO molecule on the $NiMoO_4$ (110) surface.

In the following, the adsorption of OH adsorbed on the oxygen-deficient $NiMoO_4$ (110) surface was evaluated. Specifically, the adsorption on the Ni and Mo sites with lower coordination due to the removal of surface O was considered. Interestingly, it is noted that the OH group was preferred to be adsorbed at the vicinity of the oxygen-vacancy position (Figure 9a), leading to an E_{ads} of −3.63 eV and a charge transfer at the OH/$NiMoO_4$ interface (Figure 9b). This result suggests that the presence of surface oxygen vacancies offers more active sites for OH adsorption, concentration, and subsequent redox reactions for enhanced pseudocapacitive charge storage.

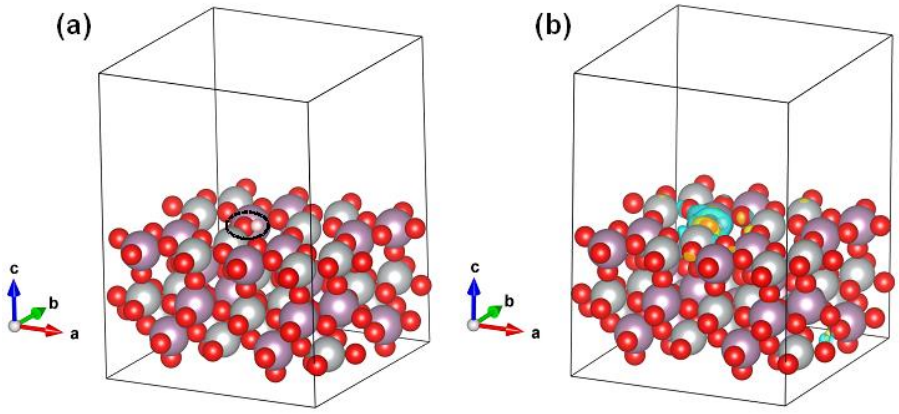

Figure 9. The optimized adsorption configurations of one HO molecule anchored on $NiMoO_4$ (110) surfaces with one surface oxygen vacancy (V_o), leading to an E_{ads} of −3.63 eV. The black dotted ellipsoid in (**a**) labels the position of the adsorbed HO molecule, which is at the vicinity of the V_o. The yellow and cyan colors in the charge density difference contour (**b**) represent the electron accumulation and depletion, respectively. The isosurface level is 0.001 e $bohr^{-3}$.

Based on the above experimental data and theoretical simulations, the significantly improved electrochemical performances of the $NiMoO_{4-x}$@C composite can be mainly attributed to the following points: (i) the deposition of amorphous carbon shell effectively enhances the electron transport of $NiMoO_4$ nanowires and charge transfer at $NiMoO_4$/C

heterointerface; (ii) the deposited carbon layer also improves the structural integrity of the $NiMoO_4$ nanowire arrays during long-term electrochemical cycling; (iii) the creation of oxygen vacancies in $NiMoO_4$ accompanied by the coating of the carbon further enhances the electronic conductivity of the $NiMoO_4$ electrode and creates more active sites for pseudocapacitive charge storage. Therefore, the synergy of defect and interface engineering of $NiMoO_4$ NWAs realized by carbon deposition effectively improves the overall electrochemical performance of the resultant $NiMoO_{4-x}$@C composite electrode in supercapacitors.

To further assess the practical application potential of a $NiMoO_{4-x}$@C sample, an asymmetric supercapacitor device ($NiMoO_{4-x}$@C//AC) was assembled with the $NiMoO_{4-x}$@C as a positive electrode and activated carbon (AC) as a negative electrode. Before testing the ASC device, we performed the CV measurements of $NiMoO_{4-x}$@C and AC electrodes in a three-electrode system at a scan rate of 5 mV s^{-1} to estimate the suitable operating voltage range (Figure 10a). The maximum operating voltage of $NiMoO_{4-x}$@C//AC ASC was determined to be 1.6 V. The CV curves of $NiMoO_{4-x}$@C//AC ASC at different scan rates are shown in Figure 10b. All the curves display obvious redox peaks, indicating the main contribution from pseudocapacitance. An increased separation of redox peak position can be noted along with the increase of scan rates due to the increased polarization. Figure 10c shows the GCD curves of the $NiMoO_{4-x}$@C//AC ASC at different current densities while Figure 10d shows the specific capacitance calculated from different current densities. The overall capacitance of the ASC was calculated to be 1.01 F cm^{-2} (156.25 F g^{-1}) at 1 mA cm^{-2}. Furthermore, the $NiMoO_{4-x}$@C//AC ASC device has demonstrated a good capacitance retention of 83.6% after 6000 cycles at 20 mA cm^{-2} (Figure 10e). As a result, the ASC device can power a yellow LED (inset of Figure 10e), showing its potential in practical applications. In addition, the electrochemical performances of our $NiMoO_{4-x}$@C//AC ASC device are also superior or comparable to some recently reported $NiMoO_4$-based electrode materials for ASCs as summarized in Table S1.

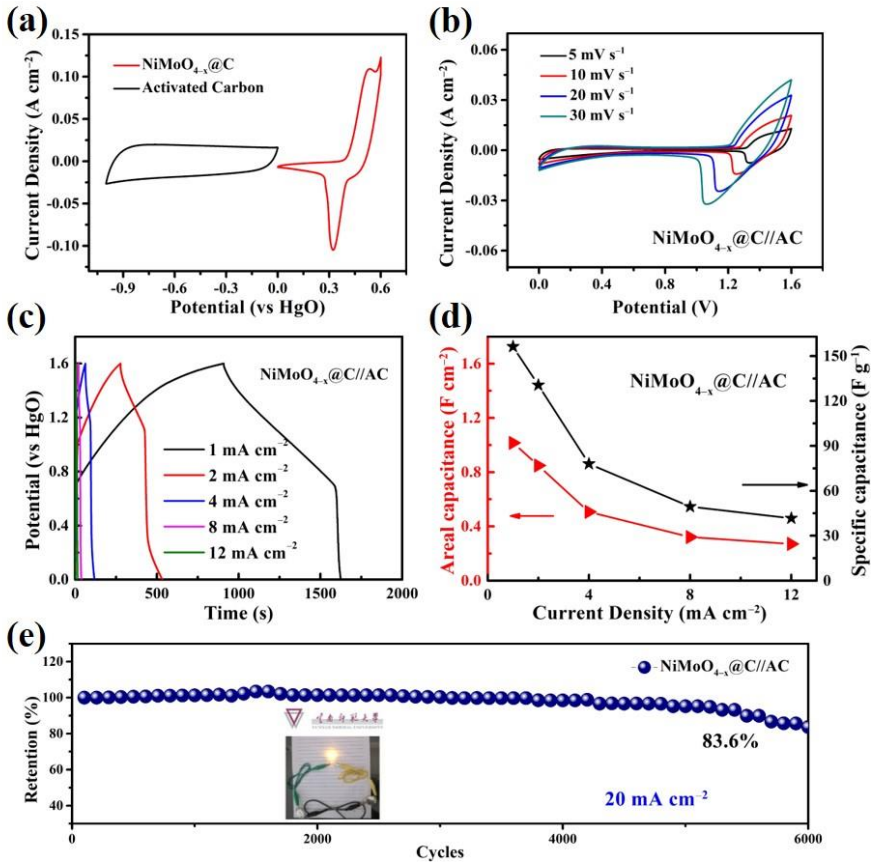

Figure 10. Electrochemical performance of the asymmetric $NiMoO_{4-x}$@C//AC supercapacitor. (**a**) CV curves of activated carbon (AC) and $NiMoO_{4-x}$@C electrodes from −1.0~0 V and 0~0.6 V, respectively

at 5 m V s^{-1}; (**b**) CV curves; (**c**) GCD curves; (**d**) areal capacitance and specific capacitance; (**e**) cyclic stability of $NiMoO_{4-x}$@C//AC.

3. Conclusions

In summary, synchronous defect and interface engineering was implemented in $NiMoO_4$ material via the formation of oxygen vacancies and the coating of the carbon on $NiMoO_4$ nanowire arrays through a simple hydrothermal method paired with sucrose pyrolysis. During this process, an amorphous carbon layer was homogeneously deposited on the surface of $NiMoO_4$ nanowires and oxygen vacancies were created on the $NiMoO_4$ surface during the carbonization of sucrose. The deposited carbon layer and formed oxygen vacancies in $NiMoO_4$ boosted the electronic conductivity of $NiMoO_4$ nanowires. In addition, the coated carbon layer also improved the structural integrity of the $NiMoO_4$ electrode during long-term operation in supercapacitors. Consequently, the resultant $NiMoO_{4-x}$@C heterostructure electrode achieved a high specific capacitance of 2.24 F cm^{-2} (1720 F g^{-1}) and maintained a good capacitance retention of about 83.6% after 6000 cycles at 20 mA cm^{-2}. In addition, the as-assembled $NiMoO_{4-x}$@C//activated carbon asymmetric supercapacitor device manifested a high energy density of 51.6 W h kg^{-1} at a high power density of 203.95 W kg^{-1}, indicating that $NiMoO_{4-x}$@C composite is a suitable electrode material for supercapacitor applications. The proposed synergistic defect and interface engineering strategy herein can be extended for the design and development of other novel composite electrode materials for applications in electrochemical energy storage and conversion.

Supplementary Materials: The following supporting information can be downloaded at https://www.mdpi.com/article/10.3390/nano12071094/s1, Figure S1: The EDS analysis of $NiMoO_{4-x}$@C composite and $NiMoO_4$ NWAs, Figure S2: SEM images of the $NiMoO_{4-x}$@C composite prepared under different annealing temperature: (a) 200 °C, (b) 400 °C, (c) 600 °C and (d) 800 °C, Figure S3: Thermogravimetric (TG) and differential scanning calorimetry (DSC) analysis of sucrose in Ar atmosphere at a ramping rate of 10 °C min^{-1}, Figure S4: (a) CV and (b) GCD of $NiMoO_{4-x}$@C samples prepared under different annealing temperatures, Figure S5: SEM images of the (a) $NiMoO_{4-x}$@C and (b) $NiMoO_4$ NWAs electrodes after 10,000 cycles at 20 mA cm^{-2}, Figure S6: Optimized geometry structures of the (a) pristine $NiMoO_4$ (110) surface and (b) oxygen-deficient $NiMoO_4$ (110) surface obtained by removing one surface O atom (green). The grey, light pink and red balls represent the Ni, Mo and O atoms, respectively [60–63], Figure S7: Charge density difference contours of after adsorption of one HO molecule on (a) Mo- and (b) Ni-side of $NiMoO_4$ (110) surface, respectively. The yellow and cyan colors denote the electron gain and loss, respectively. The isosurface level is 0.001 e $bohr^{-3}$, Table S1: Brief comparison of electrochemical performance of current work with recently relevant literature [20,22,30,55,64–72].

Author Contributions: Conceptualization, C.Q. and P.W.; methodology, P.W. and X.D.; software, R.Z. and H.-E.W.; validation, P.W., X.D. and R.Z.; formal analysis, P.W., X.D. and C.Q.; investigation, P.W. and X.D.; resources, C.Q., H.-E.W. and Y.L.; data curation, P.W., C.Q. and H.-E.W.; writing—original draft preparation, P.W.; writing—review and editing, C.Q., T.Z. and H.-E.W.; visualization, P.W. and R.Z.; supervision, C.Q. and H.-E.W.; project administration, C.Q. and Y.L.; funding acquisition, C.Q. and H.-E.W. All authors have read and agreed to the published version of the manuscript.

Funding: This work is supported by the National Natural Science Foundation of China (Grant No. 52162037) and Yunnan Fundamental Research Projects (grant No. 2019FD113 & 202101AT070120).

Data Availability Statement: All data included in this study are available upon request by contact with the corresponding author.

Conflicts of Interest: The authors declare no conflict of interest.

References

1. Augustyn, V.; Simon, P.; Dunn, B. Pseudocapacitive oxide materials for high-rate electrochemical energy storage. *Energy Environ. Sci.* **2014**, *7*, 1597–1614. [CrossRef]
2. Ma, H.N.; He, J.; Xiong, D.B.; Wu, J.S.; Li, Q.Q.; Dravid, V.; Zhao, Y.F. Nickel Cobalt Hydroxide Reduced Graphene Oxide Hybrid Nanolayers for High Performance Asymmetric Supercapacitors with Remarkable Cycling Stability. *ACS Appl. Mater. Interfaces* **2016**, *8*, 1992–2000. [CrossRef] [PubMed]
3. Yun, Q.B.; Lu, Q.P.; Zhang, X.; Tan, C.L.; Zhang, H. Three-Dimensional Architectures Constructed from Transition-Metal Dichalcogenide Nanomaterials for Electrochemical Energy Storage and Conversion. *Angew. Chem. Int. Ed.* **2018**, *57*, 626–646. [CrossRef] [PubMed]
4. Miao, C.X.; Zhou, C.L.; Wang, H.E.; Zhu, K.; Ye, K.; Wang, Q.; Yan, J.; Cao, D.X.; Li, N.; Wang, G.L. Hollow Co-Mo-Se nanosheet arrays derived from metal-organic framework for high-performance supercapacitors. *J. Power Sources* **2021**, *490*, 229532. [CrossRef]
5. Lukatskaya, M.R.; Kota, S.; Lin, Z.F.; Zhao, M.Q.; Shpigel, N.; Levi, M.D.; Halim, J.; Taberna, P.L.; Barsoum, M.; Simon, P.; et al. Ultra-high-rate pseudocapacitive energy storage in two-dimensional transition metal carbides. *Nat. Energy* **2017**, *2*, 17105. [CrossRef]
6. Ren, J.; Shen, M.; Li, Z.L.; Yang, C.M.; Liang, Y.; Wang, H.E.; Li, J.H.; Li, N.; Qian, D. Towards high-performance all-solid-state asymmetric supercapacitors: A hierarchical doughnut-like Ni_3S_2 PPy core-shell heterostructure on nickel foam electrode and density functional theory calculations. *J. Power Sources* **2021**, *501*, 230003. [CrossRef]
7. Sun, L.; Sun, Y.D.; Fu, Q.; Pan, C.X. Facile preparation of NiO nanoparticles anchored on N/P-codoped 3D carbon nanofibers network for high-performance asymmetric supercapacitors. *J. Alloys Compd.* **2021**, *888*, 161488. [CrossRef]
8. Liu, Y.; Wang, Y.F.; Meng, Y.; Plamthottam, R.; Tjiu, W.W.; Zhang, C.; Liu, T.X. Ultrathin Polypyrrole Layers Boosting MoO_3 as Both Cathode and Anode Materials for a 2.0 V High-Voltage Aqueous Supercapacitor. *ACS Appl. Mater. Interfaces* **2022**, *14*, 4490–4499. [CrossRef]
9. Shu, T.; Wang, H.; Li, Q.; Feng, Z.P.; Wei, F.X.; Yao, K.X.; Sun, Z.; Qi, J.Q.; Sui, Y.W. Highly stable Co_3O_4 nanoparticles/carbon nanosheets array derived from flake-like ZIF-67 as an advanced electrode for supercapacacitor. *Chem. Eng. J.* **2021**, *419*, 129631. [CrossRef]
10. Pandit, B.; Goda, E.S.; Abu Elella, M.H.; Rehman, A.U.; Hong, S.E.; Rondiya, S.R.; Barkataki, P.; Shaikh, S.F.; Al-Enizi, A.M.; El-Bahy, S.M.; et al. One-pot hydrothermal preparation of hierarchical manganese oxide nanorods for high-performance symmetric supercapacitors. *J. Energy Chem.* **2022**, *65*, 116–126. [CrossRef]
11. Wei, S.; Wan, C.C.; Zhang, L.Y.; Liu, X.Y.; Tian, W.Y.; Su, J.H.; Cheng, W.J.; Wu, Y.Q. N-doped and oxygen vacancy-rich $NiCo_2O_4$ nanograss for supercapacitor electrode. *Chem. Eng. J.* **2022**, *429*, 132242. [CrossRef]
12. Liu, C.X.; Zhao, Z.; Liu, Y.; Lu, Q.S. Carbon dots decorated zinc cobaltite nanowires-assembled hierarchical arrays supported on nickel foam as binder-free electrodes for high performance supercapacitors. *J. Power Sources* **2022**, *519*, 230780. [CrossRef]
13. Liu, H.Q.; Dai, M.Z.; Zhao, D.P.; Wu, X.; Wang, B. Realizing Superior Electrochemical Performance of Asymmetric Capacitors through Tailoring Electrode Architectures. *ACS Appl. Energy Mater.* **2020**, *3*, 7004–7010. [CrossRef]
14. Li, P.X.; Ruan, C.H.; Xu, J.; Xie, Y.B. Supercapacitive performance of $CoMoO_4$ with oxygen vacancy porous nanosheet. *Electrochim. Acta* **2020**, *330*, 135334. [CrossRef]
15. Zhu, Z.; Sun, Y.; Li, C.S.; Yang, C.; Li, L.; Zhu, J.H.; Chou, S.L.; Wang, M.M.; Wang, D.D.; Li, Y.L. Mini-review: Progress on micro/nanoscale $MnMoO_4$ as an electrode material for advanced supercapacitor applications. *Mater. Chem. Front.* **2021**, *5*, 7403–7418. [CrossRef]
16. Guo, D.; Zhang, P.; Zhang, H.M.; Yu, X.Z.; Zhu, J.; Li, Q.H.; Wang, T.H. $NiMoO_4$ nanowires supported on Ni foam as novel advanced electrodes for supercapacitors. *J. Mater. Chem. A* **2013**, *1*, 9024–9027. [CrossRef]
17. Denis, D.K.; Sun, X.; Zhang, J.Y.; Wang, Y.Y.; Hou, L.R.; Li, J.; Yuan, C.Z. Solid Solution Engineering of Co-Ni-Based Ternary Molybdate Nanorods toward Hybrid Supercapacitors and Lithium-Ion Batteries as High-Performance Electrodes. *ACS Appl. Energy Mater.* **2020**, *3*, 3955–3965. [CrossRef]
18. Guo, D.; Luo, Y.Z.; Yu, X.Z.; Li, Q.H.; Wang, T.H. High performance $NiMoO_4$ nanowires supported on carbon cloth as advanced electrodes for symmetric supercapacitors. *Nano Energy* **2014**, *8*, 174–182. [CrossRef]
19. Hong, J.; Lee, Y.W.; Hou, B.; Ko, W.; Lee, J.; Pak, S.; Hong, J.; Morris, S.M.; Cha, S.; Sohn, J.I.; et al. Solubility-Dependent $NiMoO_4$ Nanoarchitectures: Direct Correlation between Rationally Designed Structure and Electrochemical Pseudokinetics. *ACS Appl. Mater. Interfaces* **2016**, *8*, 35227–35234. [CrossRef]
20. Peng, S.J.; Li, L.L.; Wu, H.B.; Madhavi, S.; Lou, X.W. Controlled Growth of $NiMoO_4$ Nanosheet and Nanorod Arrays on Various Conductive Substrates as Advanced Electrodes for Asymmetric Supercapacitors. *Adv. Energy Mater.* **2015**, *5*, 1401172. [CrossRef]
21. Yin, Z.X.; Zhang, S.; Chen, Y.J.; Gao, P.; Zhu, C.L.; Yang, P.P.; Qi, L.H. Hierarchical nanosheet-based $NiMoO_4$ nanotubes: Synthesis and high supercapacitor performance. *J. Mater. Chem. A* **2015**, *3*, 739–745. [CrossRef]
22. Lin, L.Y.; Liu, T.M.; Liu, J.L.; Sun, R.; Hao, J.H.; Ji, K.M.; Wang, Z.C. Facile synthesis of groove-like $NiMoO_4$ hollow nanorods for high-performance supercapacitors. *Appl. Surf. Sci.* **2016**, *360*, 234–239. [CrossRef]
23. Yao, M.M.; Hu, Z.H.; Liu, Y.F.; Liu, P.P. A novel synthesis of size-controllable mesoporous $NiMoO_4$ nanospheres for supercapacitor applications. *Ionics* **2016**, *22*, 701–709. [CrossRef]
24. Jinlong, L.; Meng, Y.; Tongxiang, L. Enhanced performance of $NiMoO_4$ nanoparticles and quantum dots and reduced nanohole graphene oxide hybrid for supercapacitor applications. *Appl. Surf. Sci.* **2017**, *419*, 624–630. [CrossRef]

25. Huang, L.; Xiang, J.W.; Zhang, W.; Chen, C.J.; Xu, H.H.; Huang, Y.H. 3D interconnected porous $NiMoO_4$ nanoplate arrays on Ni foam as high-performance binder-free electrode for supercapacitors. *J. Mater. Chem. A* **2015**, *3*, 22081–22087. [CrossRef]
26. Wang, Z.J.; Wei, G.J.; Du, K.; Zhao, X.X.; Liu, M.; Wang, S.T.; Zhou, Y.; An, C.H.; Zhang, J. Ni Foam-Supported Carbon-Sheathed $NiMoO_4$ Nanowires as Integrated Electrode for High-Performance Hybrid Supercapacitors. *ACS Sustain. Chem. Eng.* **2017**, *5*, 5964–5971. [CrossRef]
27. Xu, Y.K.; Xuan, H.C.; Gao, J.H.; Liang, T.; Han, X.K.; Yang, J.; Zhang, Y.Q.; Li, H.; Han, P.D.; Du, Y.W. Hierarchical three-dimensional $NiMoO_4$-anchored rGO/Ni foam as advanced electrode material with improved supercapacitor performance. *J. Mater. Sci.* **2018**, *53*, 8483–8498. [CrossRef]
28. Huang, Z.Y.; Zhang, Z.; Qi, X.; Ren, X.H.; Xu, G.H.; Wan, P.B.; Sun, X.M.; Zhang, H. Wall-like hierarchical metal oxide nanosheet arrays grown on carbon cloth for excellent supercapacitor electrodes. *Nanoscale* **2016**, *8*, 13273–13279. [CrossRef]
29. Huang, Y.P.; Cui, F.; Zhao, Y.; Lian, J.B.; Bao, J.; Liu, T.X.; Li, H.M. $NiMoO_4$ nanorod deposited carbon sponges with ant-nest-like interior channels for high-performance pseudocapacitors. *Inorg. Chem. Front.* **2018**, *5*, 1594–1601. [CrossRef]
30. Murugan, E.; Govindaraju, S.; Santhoshkumar, S. Hydrothermal synthesis, characterization and electrochemical behavior of $NiMoO_4$ nanoflower and $NiMoO_4$/rGO nanocomposite for high-performance supercapacitors. *Electrochim. Acta* **2021**, *392*, 138973. [CrossRef]
31. Huang, B.J.; Yao, D.C.; Yuan, J.J.; Tao, Y.R.; Yin, Y.X.; He, G.Y.; Chen, H.Q. Hydrangea-like $NiMoO_4$-Ag/rGO as Battery-type electrode for hybrid supercapacitors with superior stability. *J. Colloid Interf. Sci.* **2022**, *606*, 1652–1661. [CrossRef] [PubMed]
32. Yao, P.P.; Li, C.Y.; Yu, J.L.; Zhang, S.; Zhang, M.; Liu, H.C.; Ji, M.W.; Cong, G.T.; Zhang, T.; Zhu, C.Z.; et al. High performance flexible energy storage device based on copper foam supported $NiMoO_4$ nanosheets-CNTs-CuO nanowires composites with core-shell holey nanostructure. *J. Mater. Sci. Technol.* **2021**, *85*, 87–94. [CrossRef]
33. Zhu, D.; Sun, X.; Yu, J.; Liu, Q.; Liu, J.Y.; Chen, R.R.; Zhang, H.S.; Song, D.L.; Li, R.M.; Wang, J. Three-dimensional heterostructured polypyrrole/nickel molybdate anchored on carbon cloth for high-performance flexible supercapacitors. *J. Colloid Interf. Sci.* **2020**, *574*, 355–363. [CrossRef] [PubMed]
34. Hao, Y.Y.; Huang, H.; Wang, Q.Q.; Wang, Q.; Zhou, G.W. Nitrogen-doped carbon/$NiMoO_4$ nanospheres assembled by nanosheets and ultrasmall nanoparticles for supercapacitors. *Chem. Phys. Lett.* **2019**, *728*, 215–223. [CrossRef]
35. Tong, B.L.; Wei, W.T.; Chen, X.L.; Wang, J.; Ye, W.Y.; Cui, S.Z.; Chen, W.H.; Mi, L.W. Designed synthesis of porous $NiMoO_4$/C composite nanorods for asymmetric supercapacitors. *Cryst. Eng. Comm.* **2019**, *21*, 5492–5499. [CrossRef]
36. Li, Y.; Zhang, S.M.; Ma, M.Y.; Mu, X.M.; Zhang, Y.X.; Du, J.W.; Hu, Q.; Huang, B.Y.; Hua, X.H.; Liu, G.; et al. Manganese-doped nickel molybdate nanostructures for high-performance asymmetric supercapacitors. *Chem. Eng. J.* **2019**, *372*, 452–461. [CrossRef]
37. Yuan, J.J.; Yao, D.C.; Jiang, L.; Tao, Y.R.; Che, J.F.; He, G.Y.; Chen, H.Q. Mn-Doped $NiMoO_4$ Mesoporous Nanorods/Reduced Graphene Oxide Composite for High-Performance All-Solid-State Supercapacitor. *ACS Appl. Energy Mater.* **2020**, *3*, 1794–1803. [CrossRef]
38. Wang, F.F.; Ma, K.; Tian, W.; Dong, J.C.; Han, H.; Wang, H.P.; Deng, K.; Yue, H.R.; Zhang, Y.X.; Jiang, W.; et al. P-Doped $NiMoO_4$ parallel arrays anchored on cobalt carbonate hydroxide with oxygen vacancies and mass transfer channels for supercapacitors and oxygen evolution. *J. Mater. Chem. A* **2019**, *7*, 19589–19596. [CrossRef]
39. Sharma, P.; Sundaram, M.M.; Watcharatharapong, T.; Laird, D.; Euchner, H.; Ahuja, R. Zn Metal Atom Doping on the Surface Plane of One-Dimesional $NiMoO_4$ Nanorods with Improved Redox Chemistry. *ACS Appl. Mater. Interfaces* **2020**, *12*, 44815–44829. [CrossRef]
40. Cui, S.Z.; Wang, F.Q.; Sun, K.J.; Wang, X.; Hu, Q.Z.; Peng, H.; Ma, G.F.; Lei, Z.Q. High-Performance Hybrid Supercapacitors Based on Ce-Doped $NiMoO_4$ Nanosheets and Fe_3O_4@Bi_2O_3 Nanoarrays. *J. Phys. Chem. C* **2021**, *125*, 18129–18140. [CrossRef]
41. Qing, C.; Yang, C.X.; Chen, M.Y.; Li, W.H.; Wang, S.Y.; Tang, Y.W. Design of oxygen-deficient $NiMoO_4$ nanoflake and nanorod arrays with enhanced supercapacitive performance. *Chem. Eng. J.* **2018**, *354*, 182–190. [CrossRef]
42. Sivakumar, P.; Raj, C.J.; Park, J.; Jung, H. Synergistic effects of nanoarchitecture and oxygen vacancy in nickel molybdate hollow sphere towards a high-performance hybrid supercapacitor. *Int. J. Energy Res.* **2021**, *45*, 21516–21526. [CrossRef]
43. Zhu, S.; Le, J.Y.; Mao, Y.J.; Chen, S.X.; Han, X.X.; Zeng, Z.L.; Wang, J.; Deng, S.G. Synergistic engineering of fluorine doping and oxygen vacancies towards high-energy and long-lifespan flexible solid-state asymmetric supercapacitor. *Ionics* **2021**, *27*, 2649–2658. [CrossRef]
44. Zhang, X.Y.; Wei, L.; Guo, X. Ultrathin mesoporous $NiMoO_4$-modified MoO_3 core/shell nanostructures: Enhanced capacitive storage and cycling performance for supercapacitors. *Chem. Eng. J.* **2018**, *353*, 615–625. [CrossRef]
45. Shen, J.W.; Wang, Q.G.; Zhang, K.; Wang, S.M.; Li, L.; Dong, S.B.; Zhao, S.T.; Chen, J.; Sun, R.S.; Wang, Y.; et al. Flexible carbon cloth based solid-state supercapacitor from hierarchical holothurian-morphological $NiCo_2O_4$@$NiMoO_4$/PANI. *Electrochim. Acta* **2019**, *320*, 134578. [CrossRef]
46. Xu, R.; Lin, J.M.; Wu, J.H.; Huang, M.L.; Fan, L.Q.; Xu, Z.D.; Song, Z.Y. A high-performance pseudocapacitive electrode material for supercapacitors based on the unique $NiMoO_4$/NiO nanoflowers. *Appl. Surf. Sci.* **2019**, *463*, 721–731. [CrossRef]
47. Yu, D.Y.; Zhang, Z.Q.; Teng, Y.F.; Meng, Y.N.; Wu, Y.P.; Liu, X.L.; Hua, Y.J.; Zhao, X.D.; Liu, X.Y. Fabrication of CuO@$NiMoO_4$ core-shell nanowire arrays on copper foam and their application in high-performance all-solid-state asymmetric supercapacitors. *J. Power Sources* **2019**, *440*, 227164. [CrossRef]

48. Liu, Y.; Ma, Z.L.; Xin, N.; Ying, Y.L.; Shi, W.D. High-performance supercapacitor based on highly active P-doped one-dimension/two-dimension hierarchical $NiCo_2O_4/NiMoO_4$ for efficient energy storage. *J. Colloid Interf. Sci.* **2021**, *601*, 793–802. [CrossRef]
49. Zeng, Y.; Liao, J.Z.; Wei, B.B.; Huang, Z.; Zhu, W.J.; Zheng, J.X.; Liang, H.F.; Zhang, Y.Z.; Wang, Z.C. Tuning the electronic structure of $NiMoO_4$ by coupling with SnO2 for high-performance hybrid supercapacitors. *Chem. Eng. J.* **2021**, *409*, 128297. [CrossRef]
50. Chen, C.; Yan, D.; Luo, X.; Gao, W.J.; Huang, G.J.; Han, Z.W.; Zeng, Y.; Zhu, Z.H. Construction of Core-Shell $NiMoO_4$@Ni-Co-S Nanorods as Advanced Electrodes for High-Performance Asymmetric Supercapacitors. *ACS Appl. Mater. Interfaces* **2018**, *10*, 4662–4671. [CrossRef]
51. Chen, F.S.; Ji, S.; Liu, Q.B.; Wang, H.; Liu, H.; Brett, D.J.L.; Wang, G.X.; Wang, R.F. Rational Design of Hierarchically Core-Shell Structured Ni_3S_2@$NiMoO_4$ Nanowires for Electrochemical Energy Storage. *Small* **2018**, *14*, 1800791. [CrossRef] [PubMed]
52. Acharya, J.; Ojha, G.P.; Kim, B.S.; Pant, B.; Park, M. Modish Designation of Hollow-Tubular rGO-$NiMoO_4$@Ni-Co-S Hybrid Core-shell Electrodes with Multichannel Superconductive Pathways for High-Performance Asymmetric Supercapacitors. *ACS Appl. Mater. Interfaces* **2021**, *13*, 17487–17500. [CrossRef] [PubMed]
53. Hu, K.L.; Jeong, S.; Elumalai, G.; Kukunuri, S.; Fujita, J.; Ito, Y. Phase-Dependent Reactivity of Nickel Molybdates for Electrocatalytic Urea Oxidation. *ACS Appl. Energy Mater.* **2020**, *3*, 7535–7542. [CrossRef]
54. Wang, Y.; Liu, J.; Chen, X.; Kang, B.; Wang, H.-E.; Xiong, P.; Chen, Q.; Wei, M.; Li, N.; Qian, Q.; et al. Structural engineering of tin sulfides anchored on nitrogen/phosphorus dual-doped carbon nanofibres in sodium/potassium-ion batteries. *Carbon* **2022**, *189*, 46–56. [CrossRef]
55. Nti, F.; Anang, D.A.; Han, J.I. Facilely synthesized $NiMoO_4/CoMoO_4$ nanorods as electrode material for high performance supercapacitor. *J. Alloys Compd.* **2018**, *742*, 342–350. [CrossRef]
56. Zhang, Z.; Liu, Y.; Huang, Z.; Ren, L.; Qi, X.; Wei, X.; Zhong, J. Facile hydrothermal synthesis of $NiMoO_4$@$CoMoO_4$ hierarchical nanospheres for supercapacitor applications. *Phys. Chem. Chem. Phys.* **2015**, *17*, 20795–20804. [CrossRef]
57. Zhao, X.; Wang, H.E.; Chen, X.X.; Cao, J.; Zhao, Y.D.; Neale, Z.G.; Cai, W.; Sui, J.H.; Cao, G.Z. Tubular MoO_2 organized by 2D assemblies for fast and durable alkali-ion storage. *Energy Storage Mater.* **2018**, *11*, 161–169. [CrossRef]
58. Wang, H.E.; Zhao, X.; Yin, K.L.; Li, Y.; Chen, L.H.; Yang, X.Y.; Zhang, W.J.; Su, B.L.; Cao, G.Z. Superior Pseudocapacitive Lithium-Ion Storage in Porous Vanadium Oxides C Heterostructure Composite. *ACS Appl. Mater. Interfaces* **2017**, *9*, 43665–43673. [CrossRef]
59. Wang, H.E.; Yin, K.L.; Qin, N.; Zhao, X.; Xia, F.J.; Hu, Z.Y.; Guo, G.L.; Cao, G.Z.; Zhang, W.J. Oxygen-deficient titanium dioxide as a functional host for lithium-sulfur batteries. *J. Mater. Chem. A* **2019**, *7*, 10346–10353. [CrossRef]
60. Perdew, J.P.; Burke, K.; Ernzerhof, M. Generalized Gradient Approximation Made Simple. *Phys. Rev. Lett.* **1996**, *77*, 3865–3868. [CrossRef]
61. Kresse, G.; Joubert, D. From ultrasoft pseudopotentials to the projector augmented-wave method. *Phys. Rev. B* **1999**, *59*, 1758–1775. [CrossRef]
62. Momma, K.; Izumi, F. VESTA 3 for three-dimensional visualization of crystal, volumetric and morphology data. *J. Appl. Cryst.* **2011**, *44*, 1272–1276. [CrossRef]
63. Wang, V.; Xu, N.; Liu, J.C.; Tang, G.; Geng, W.T. VASPKIT: A user-friendly interface facilitating high-throughput computing and analysis using VASP code. *Comp. Phys. Comm.* **2021**, *267*, 108033. [CrossRef]
64. Zhao, Y.; Zhang, P.; Fu, W.; Ma, X.; Zhou, J.; Zhang, X.; Li, J.; Xie, E.; Pan, X. Understanding the role of Co_3O_4 on stability between active hierarchies and scaffolds: An insight into $NiMoO_4$ composites for supercapacitors. *Appl. Surf. Sci.* **2017**, *416*, 160–167. [CrossRef]
65. Xuan, H.; Xu, Y.; Zhang, Y.; Li, H.; Han, P.; Du, Y. One-step combustion synthesis of porous CNTs/C/$NiMoO_4$ composites for high-performance asymmetric supercapacitors. *J. Alloys Compd.* **2018**, *745*, 135–146. [CrossRef]
66. Huang, Y.; Cui, F.; Zhao, Y.; Lian, J.; Bao, J.; Li, H. Controlled growth of ultrathin $NiMoO_4$ nanosheets on carbon nanofiber membrane as advanced electrodes for asymmetric supercapacitors. *J. Alloys Compd.* **2018**, *753*, 176–185. [CrossRef]
67. Hussain, S.; Javed, M.S.; Asim, S.; Shaheen, A.; Khan, A.J.; Abbas, Y.; Ullah, N.; Iqbal, A.; Wang, M.; Qiao, G. Novel gravel-like $NiMoO_4$ nanoparticles on carbon cloth for outstanding supercapacitor applications. *Ceram. Int.* **2020**, *46*, 6406–6412. [CrossRef]
68. Feng, X.; Ning, J.; Wang, D.; Zhang, J.; Xia, M.; Wang, Y.; Hao, Y. Heterostructure arrays of $NiMoO_4$ nanoflakes on N-doping of graphene for high-performance asymmetric supercapacitors. *J. Alloys Compd.* **2020**, *816*, 152625. [CrossRef]
69. Zhong, Y.; Liu, T.; Zhang, A.; Cui, L.; Liu, X.; Zheng, R.; Liu, J. Controllable synthesis of $Ni_{1-x}Co_xMoO_4$ with tunable morphologies for high-performance asymmetric supercapacitors. *J. Alloys Compd.* **2021**, *850*, 156734. [CrossRef]
70. Chen, L.; Deng, W.; Chen, Z.; Wang, X. Hetero-architectured core–shell $NiMoO_4$@Ni_9S_8/MoS_2 nanorods enabling high-performance supercapacitors. *J. Mater. Res.* **2022**, *37*, 284–293. [CrossRef]
71. Muthu, D.; Vargheese, S.; Haldorai, Y.; Kumar, R.T.R. $NiMoO_4$/reduced graphene oxide composite as an electrode material for hybrid supercapacitor. *Mater. Sci. Semicond. Proc.* **2021**, *135*, 106078. [CrossRef]
72. Yi, T.-F.; Qiu, L.-Y.; Mei, J.; Qi, S.-Y.; Cui, P.; Luo, S.; Zhu, Y.-R.; Xie, Y.; He, Y.-B. Porous spherical NiO@$NiMoO_4$@PPy nanoarchitectures as advanced electrochemical pseudocapacitor materials. *Sci. Bull.* **2020**, *65*, 546–556. [CrossRef]